bioRxiv preprint doi: https://doi.org/10.1101/174599; this version posted August 10, 2017. The copyright holder for this preprint (which was not certified by peer review) is the author/funder, who has granted bioRxiv a license to display the preprint in perpetuity. It is made available under aCC-BY-NC-ND 4.0 International license.

Cell growth rate dictates the onset of glass to fluid-like transition and long time super-diffusion in an evolving cell colony

Abdul N Malmi-Kakkada[1], Xin Li[1], Himadri S. Samanta[1], Sumit Sinha[2], D. Thirumalai[1]*
[1] *Department of Chemistry, University of Texas, Austin, TX 78712, USA. and*
[2] *Department of Physics, University of Texas, Austin, TX 78712, USA.*
(Dated: August 7, 2017)

Collective migration dominates many phenomena, from cell movement in living systems to abiotic self-propelling particles. Focusing on the early stages of tumor evolution, we enunciate the principles involved in cell dynamics and highlight their implications in understanding similar behavior in seemingly unrelated soft glassy materials and possibly chemokine-induced migration of $CD8^+$ T cells. We performed simulations of tumor invasion using a minimal three dimensional model, accounting for cell elasticity and adhesive cell-cell interactions to establish that cell growth rate-dependent tumor expansion results in the emergence of distinct topological niches. Cells at the periphery move with higher velocity perpendicular to the tumor boundary, while motion of interior cells is slower and isotropic. The mean square displacement, $\Delta(t)$, of cells exhibits glassy behavior at times comparable to the cell cycle time, while exhibiting super-diffusive behavior, $\Delta(t) \approx t^{\alpha}$, at longer times. We derive the value of $\alpha \approx \frac{4}{3}$ using a field theoretic approach based on stochastic quantization. In the process we establish the universality of super-diffusion in a class of seemingly unrelated non-equilibrium systems. Our findings for the collective migration, which also suggests that tumor evolution occurs in a polarized manner, are in quantitative agreement with *in vitro* experiments. Although set in the context of tumor invasion the findings should also hold in describing collective motion in growing cells and in active systems where creation and annihilation of particles play a role.

The strict control of cell division and apoptosis is critical for tissue development and maintenance [1]. Dysfunctional cell birth and death control mechanisms lead to several physiological diseases including cancers [2]. Together with genetic cues controlling birth-death processes, mechanical behavior of a collection of cells is thought to be of fundamental importance in biological processes such as embryogenesis, wound healing, stem cell dynamics, morphogenesis, tumorigenesis and metastasis [3–8]. Due to the interplay between birth-death processes and cell-cell interactions, we expect that collective motion of cells ought to exhibit unusual non-equilibrium dynamics, whose understanding might hold the key to describing tumor invasion and related phenomena. Interestingly, characteristics of glass-like behavior such as diminished motion (jamming) of a given cell in a dense environment created by neighboring cells (caging effect), dynamic heterogeneity, and possible viscoelastic response have been reported in confluent tissues [9, 10]. Using imaging techniques that track cell motions, it has been shown that in both two (kidney cells on a flat thick polyacrylamide gel [9, 11]) and three dimensions (explants from zebrafish embedded in agarose [12]) the mean displacement exhibits sub-diffusive behavior, reminiscent of dynamics in supercooled liquids at intermediate time scales. This behavior, which can be rationalized by noting that the core of a growing collection of cells is likely to be in a jammed state, is expected on time scales less than the cell division time.

A theory to capture the essence of tumor invasion must consider the interplay of the cell mechanics, adhesive interaction between cells, and the dynamics associated with cell division and apoptosis, over a wide range of time scales. In an attempt to capture collective dynamics in cells a number of models based on cellular automaton [13, 14], vertex and Voronoi models [15–18], subcellular element model [19], cell dynamics based on Potts model [20, 21], and phase field description for collective migration [22, 23] have been proposed. Previous works have investigated a number of two-dimensional (2D) models in various contexts [9, 16, 24] including probing the dynamics in a homeostatic state where cell birth-death processes are balanced [25, 26]. Existing three-dimensional (3D) models focus solely on tumor growth kinetics, spatial growth patterns [27, 28] or on cell migration at low cellular density at time regimes shorter than the cell division time [29–31]. A recent interesting study [25] shows that cell dynamics in a confluent tissue is always fluidized by cell birth and death processes, on time scales comparable to cell division time. A more recent two-dimensional model [26] investigates glass-to-liquid transition in confluent tissues. However, both these instructive models [25, 26] focus on the steady state regime where the number of tumor cells is kept constant by balancing the birth and death rates. Consequently, they do not address the non-equilibrium dynamics of the evolving tumor in the early stages, which is of great interest in cancer biology [32–34].

Here, we use a minimal physical 3D model that combines both cell mechanical characteristics, cell-cell adhesive interactions and variations in cell birth rates to probe the non-steady state tumor evolution. Such a model, which has the distinct advantage that it can be generalized to include mutational effects naturally, was first introduced by Drasdo and Höhme [27]. One of our primary

* dave.thirumalai@gmail.com

bioRxiv preprint doi: https://doi.org/10.1101/174599; this version posted August 10, 2017. The copyright holder for this preprint (which was not certified by peer review) is the author/funder, who has granted bioRxiv a license to display the preprint in perpetuity. It is made available under aCC-BY-NC-ND 4.0 International license.

goals is to understand quantitatively the complex invasion dynamics of tumor into a collagen matrix, and provide a mechanism for the observation of super-diffusive behavior. We use free boundary conditions for tumor evolution to study dynamical fingerprints of invasion in order to quantitatively compare the results to experimental observations. We model the proliferation behavior of tumor cells, and investigate the effect of pressure dependent growth inhibition. Good agreement between our results and *in vitro* experiments on three-dimensional growth of multicellular tumor spheroids lends credence to the model. On time scales less than the cell division time, the dynamics of cell movement within the tumor exhibits glassy behavior, reflected in a sub-diffusive behavior of the mean square displacement, $\Delta(t)$. However, at times exceeding cell division time $\Delta(t) \sim t^{\alpha}$ ($\alpha \approx 1.3$). The duration for which sub-diffusion persists decreases as the cell growth rate increases in sharp contrast to the dynamics in confluent tissues. Detailed analyses of individual cell trajectories reveal complex heterogeneous spatial and time dependent cell migration patterns, thus providing insights into how cells are poised for invasion into regions surrounding the tumor. We find that activity due to cell division coupled with cell mechanical interactions plays a critical role in the non-equilibrium dynamics and the physical structure of the polarized tumor invasion process. The dynamical properties of cells in our model share considerable similarities to those found in non-living soft materials such as soap foams and toothpaste [35, 36]. In all these cases the transition from a glass-like behavior to super diffusion occurs as a result of cell growth or creation of particles, resulting in non-conservation of number density. In order to describe the results as clearly as possible we have relegated all the technical details, including description of the model, the simulation methods, the theory, as well as other results that validate the major results in Appendices.

I. RESULTS

Predicted pressure-dependent growth dynamics is consistent with experiments. Visual representation of the tumor growth process generated in simulations is vividly illustrated in the movie (see Movies 1 and 2) in the Appendix E. Snapshots of the evolving collection of cells at different times is presented in Figs. 1a-d. As the tumor evolves, the cells aggregate into a spheroidal shape due to cell division plane being isotropically distributed (Fig. 1d and the movie in the Appendix E). In spheroidal cell aggregates, it is known that pressure inhibits cell proliferation [37–39]. We expect the pressure (see Appendix C for the calculations) experienced by the cells in the interior of the tumor to be elevated due to crowding effects, causing the cells to enter a dormant state if the pressure from the neighbors reaches a threshold value, p_c. Tumor growth behavior is strongly dependent on the value of p_c (see Fig. 1e). At $p_c = 10^{-3}$ MPa, the total number ($N(t)$) of tumor cells during growth is well approximated as an exponential $N(t) \propto exp(const \times t)$. As p_c is lowered, implying growth is inhibited at smaller pressures, increase in the tumor size is described by a power law, $N(t) \propto t^{\beta}$, at long timescales, while $N(t)$ retains exponential growth at early stages (see the inset of Fig. 1e). Our simulations also show that β is p_c-dependent, increasing as p_c increases. Power-law growth in 3D tumor spheroid size has been observed in many tumor cell lines with β varying from one to three [40–44]. The overall growth of the tumor slows down as the value of pressure experienced by cells increases, which is also consistent with recent experimental results [38]. The known results in Fig. 1e, which are in near quantitative agreement with several experiments, merely serve to validate the model.

Cell motility within the tumor spheroid. Using direct imaging it has become possible to monitor the overall invasion of the tumor as well as the movement of individual cells within the spheroid [45, 46]. In order to compare our results to experiments we calculated the mean square displacement, $\Delta(t) = \langle[\mathbf{r}(t) - \mathbf{r}(0)]^2\rangle$, of individual cells. By tracking the movement of all the initial cells within the tumor, we calculated $\Delta(t)$ by averaging over hundreds of trajectories. The growth rate-dependent $\Delta(t)$ (displayed in Fig. 2a on a log-log scale) shows that there is a rapid increase in $\Delta(t)$ at early times ($t \leq 0.01\tau_{min}$, where τ_{min} is the benchmark value of the cell cycle time given in Table I in the Appendix) because the cells move unencumbered, driven by repulsive interaction with other cells (see discussion about the role of initial conditions in the Appendix D). At intermediate timescales ($0.01\tau_{min} < t < \tau$ with τ being the average cell cycle time), $\Delta(t)$ exhibits sub-diffusive behavior ($\Delta(t) \sim t^{s}$ with $s < 1$). The signatures of plateaus in $\Delta(t)$ (together with other characteristics discussed later) in this time regime indicate that cells are caged by the neighbors (see the left inset in Fig. 2a), and consequently undergo only small displacements. Such a behavior is reminiscent of a supercooled liquid undergoing a glass transition, as vividly illustrated in colloidal particles using direct imaging as their densities approach the glass transition [47, 48]. As τ increases, the plateau persists for longer times because of a decrease in the outward stress, which slows the growth of the tumor. At t exceeding τ, the $\Delta(t)$ exhibits super-diffusive motion ($\Delta(t) \approx t^{\alpha}$ with $\alpha \approx 1.33$). On these time scales, cells can escape the cage, as illustrated in the middle inset of Fig. 2a. Our observation of super-diffusion in $\Delta(t)$ at long times agrees well with the experimental result ($\alpha \approx 1.4 \pm 0.04$) obtained for fibrosarcoma cells in a growing tumor spheroid [32]. The onset of super-diffusive behavior in $\Delta(t)$ shifts to earlier times as we decrease the average cell cycle time (see Fig. 2a), implying that cell division is the mechanism resulting in super-diffusion.

Theoretical predictions. In order to understand the role of cell growth and apoptosis in the observed sluggish dynamics at intermediate times and super-diffusive be-

bioRxiv preprint doi: https://doi.org/10.1101/174599; this version posted August 10, 2017. The copyright holder for this preprint (which was not certified by peer review) is the author/funder, who has granted bioRxiv a license to display the preprint in perpetuity. It is made available under aCC-BY-NC-ND 4.0 International license.

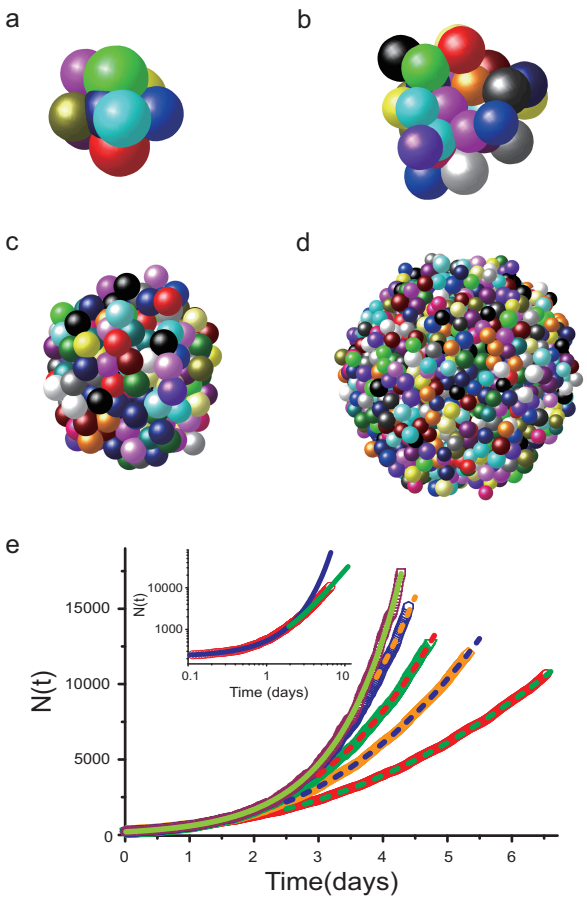

FIG. 1. **Tumor growth simulations. a-d** show instantaneous snapshots of the tumor during growth at different times. Each cell is represented by a sphere. There are approximately 2,000 cells in **d**. The color of each cell is to aid visualization. **Figures 1a-d** are rescaled for illustration purposes. Note that even at $t = 0$ the sizes of the cells are different, they are drawn from a Gaussian distribution. **e**, The total number of tumor cells, $N(t)$, as a function of time at different values of the threshold pressure p_c, which increases from bottom to top (10^{-4}, 2×10^{-4}, 3×10^{-4}, 5×10^{-4}, 10^{-3} MPa). The solid line is an exponential function while other dashed lines show power-law behavior $N(t) \approx t^{\beta}$ where β ranges from 2.2, 2.5, 2.8 to 3 (from bottom to top). The inset in **e** shows $N(t)$ with $p_c = 10^{-4}$ on a log-log scale with both exponential and power law fits. The blue curve in the inset is an exponential function while the power-law trend is illustrated by the green line. The average cell cycle time $\tau = \tau_{min} = 54{,}000$s and other parameter values are taken from Table I in the Appendix.

havior at long times, we developed a theory to study the dynamics of a colony of cells in a dissipative environment (Appendix A). The interactions between cells contain both attractive (adhesive) and excluded volume terms. Starting from the Langevin equation describing the dynamics of the ith cell, and incorporating the birth reaction, $X \xrightarrow{k_a} X + X$ with the rate constant k_a $(= 1/\tau)$ for each cell, and the apoptosis reaction $X + X \xrightarrow{k_b} X$ with the rate k_b, an equation for the time dependence of the density $\rho(\mathbf{k}, t)$ (Eq. A3 in the Appendix A) can be derived. The cell division and apoptosis processes drive the system far from equilibrium, thus violating the Fluctuation Dissipation Theorem (FDT). As a consequence, we cannot use standard methods used to compute response and correlation functions from which the t-dependence of $\Delta(t)$ can be deduced. To overcome this difficulty we used the Parisi-Wu stochastic quantization method [49] in which the evolution of $\rho(\mathbf{k}, \omega)$ (ω is the frequency) is described in a fictitious time in which FDT is preserved. From the analysis of the resulting equation (Appendix A contains the sketch of the calculations) the scaling of $\Delta(t)$ may be obtained as,

$$\Delta(t) = \langle [\mathbf{r}(t) - \mathbf{r}(0)]^2 \rangle \ \sim t^{2/z} \ . \qquad (1)$$

In the intermediate time regime, $z = 5/2$, implying $\Delta(t) \approx t^{4/5}$. The predicted sub-diffusive behavior of $\Delta(t)$ is qualitatively consistent with simulation results. It is likely that the differences in the scaling exponent between simulations ($2/z \approx 0.33$) and theoretical predictions ($2/z \approx 0.8$) in this non-universal time regime may be due to the differences in the cell-to-cell interactions used in the two models.

In the long time limit, the cell birth-death process (the fourth term in Eq. A3) dominates the interactions between cells. As a result, we expect that the exponent $2/z$ should be universal, independent of the forces governing cell motility. Our theory predicts that $z = 3/2$, which shows that $\Delta(t) \approx t^{4/3}$, in excellent agreement with the simulations (Fig. 2a) and experiments [32]. It is clear from our theory that it is the interaction-independent birth-death process that drives the *observed fluidization* during tumor (or tissue) development, resulting in super-diffusive cell motion at long times. The underlying mechanism for obtaining super-diffusive behavior is that cells must move persistently in a given direction for a long time leading to polarized tumor growth, ultimately resulting in invasion driven predominantly by birth (see below).

Dependence of relaxation times on cell cycle time. To further quantify the fluidization transition driven by cell birth-death processes, we calculated the isotropic self-intermediate scattering function $F_s(q, t) = \langle e^{i\mathbf{q}\cdot(\mathbf{r}(t)-\mathbf{r}(0))} \rangle$ at $|\mathbf{q}| = 2\pi/r_0$, where r_0 is the position of the first maximum in the pair correlation function (see Fig. 10 in Appendix D). The average is taken over all the initial cells, which are alive during the entire simulation time and the angles of $\mathbf{q}$. We note that $F_s(q, t)$ exhibits a two-step relaxation process (Fig. 2b) characterized by two time scales. The initial relaxation time, corresponding to the motion of cells in a cage formed by neighboring cells, depends only weakly on the cell cycle time. The second relaxation time (τ_α), extracted by fitting $F_s(q, t)$ to an exponential function ($F_s(q, t) \approx a_0 e^{-t/\tau_\alpha}$, see green lines in Fig. 2b), depends strongly on the average cell cycle time. As in the relaxation of supercooled liquids, τ_α is associated with the collective motion of cells leaving the cage [50, 51]. As the average cell cycle time is

bioRxiv preprint doi: https://doi.org/10.1101/174599; this version posted August 10, 2017. The copyright holder for this preprint (which was not certified by peer review) is the author/funder, who has granted bioRxiv a license to display the preprint in perpetuity. It is made available under aCC-BY-NC-ND 4.0 International license.

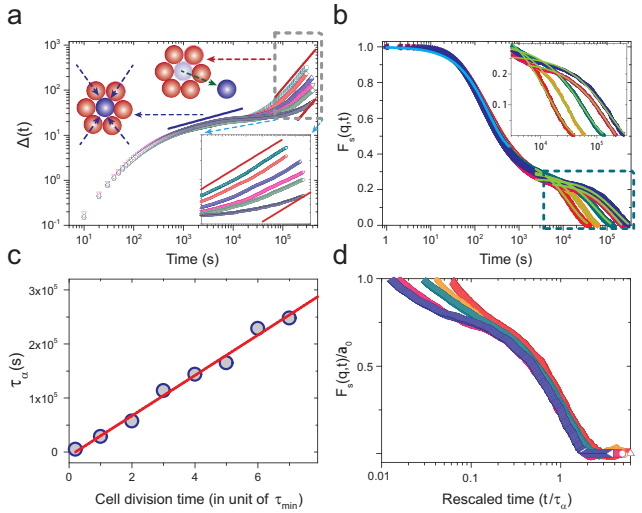

FIG. 2. **Dynamics of the tumor cells at varied cell cycle times.** **a**, The mean-squared displacement ($\Delta(t)$) of cells. From top to bottom, the curves correspond to increasing average cell cycle time (τ is varied from τ_{min} to $10\tau_{min}$ where $\tau_{min} = 54,000$ seconds). Time taken for reaching the super-diffusive regime increases by increasing τ. The blue and red lines have a slope of 0.33, and 1.3, respectively. The sub-diffusive (super-diffusive) behavior corresponds to dynamics in the intermediate (long) times. The left and middle inset illustrate the "cage effect" and "cage-jump" motion, respectively. The right inset shows a zoom-in for the dashed-line rectangle at long timescales. The unit for y-axis is (μm^2). **b**, The self-intermediate scattering function, $F_s(q,t)$, shows that relaxation occurs in two steps. From left to right, the second relaxation for $F_s(q,t)$ slows down as τ increases (from $0.5\tau_{min}$ to $5\tau_{min}$). The solid lines are exponential fits. The upper inset shows a zoom-in for the dashed-line rectangle at long timescales. **c**, The second relaxation time τ_α obtained from **b** as a function of cell division time (rescaled by τ_{min}). The red solid line is a linear fit ($\tau_\alpha \propto 0.69\tau$). **d**, The rescaled self-intermediate scattering function $F_s(q,t)/a_0$ as a function of the rescaled time t/τ_α.

reduced, τ_α decreases (see Fig. 2c), and the $F_s(q,t)$ begins to approach a single relaxation regime, as expected for a normal fluid. The second relaxation process in $F_s(q,t)$ (Fig. 2b) can be collapsed onto one master curve by rescaling time by τ_α, resulting in the independence of $F_s(q,t)$ on the cell cycle time (Fig. 2d). We surmise that the cage relaxation is driven by the same mechanism (the cell birth-death processes) that gives rise to super-diffusive behavior in $\Delta(t)$.

Heterogeneity during tumor growth. The effect of glass or liquid-like state of tumor growth is vividly illustrated by following the trajectories of individual cells in the growing tumor. Figs. 3a and 3b highlight the trajectory of cells during a time of ≈ 3 days for the average cell division time of $15\tau_{min}$ and $0.25\tau_{min}$, respectively. In the glass-like phase (intermediate times), the displacements are small, exhibiting caging behavior especially at the longer cell cycle time (Fig. 3a), resulting in the localization of the cells near their starting positions. On the other hand, cells move long distances and show signatures of persistent directed motion at the shorter cell cycle time (see Fig. 3b). These observations suggest that the anisotropic growth of cells, manifested largely in the evolution of cells at the periphery of the tumor, depends on the cell growth rate, a factor that determines tumor virulency.

Because the nature of cell movement determines cancer progression and metastasis [52], it is critical to understand how various factors affect collective cell migration emerging from individual cell movements (Figs. 3a-c). Insight into cell migrations may be obtained by using analogies to spatial heterogenous dynamics in supercooled liquids [53, 54]. In simple fluids, the distribution of particle displacement is Gaussian while in supercooled liquids the displacements of a subset of particles deviate from the Gaussian distribution [53]. In Fig. 3c, the van Hove function of cell displacement (or the probability distribution of step size) is shown. The single time step distance covered by a cell is defined as $|\delta r_i(\delta t)| = |r_i(t+\delta t) - r_i(t)|$. By analyzing $\delta r_i(\delta t = 100s)$ for all initial cells throughout the simulation, we obtain a long-tailed δr probability distribution ($P(\delta r)$), which is considerably broader than the Gaussian distribution (see Fig. 13 in Appendix D), providing one indication of heterogeneity [55]. The non-Gaussian parameter[56] $\Gamma \equiv \langle \delta r(\delta t)^4 \rangle / (3\langle \delta r(\delta t)^2 \rangle^2) - 1$ is about 200 which is far greater than 0 expected for a Gaussian distribution. The distribution $P(\delta r)$, has a broad, power law tail cut off at large values of δr, that depends on the cell cycle time. As we approach the glass-like phase for longer average cell cycle time, $P(\delta r)$ is suppressed by an order of magnitude over a wide range of δr. Interestingly, we do not observe an abrupt change in the behavior of $P(\delta r)$ as the average cell cycle time is changed. The transition between glass-like and liquid-like regimes occurs continuously.

Cell-to-cell phenotypic heterogeneity is considered to be one of the greatest challenges in cancer therapeutics [57, 58]. Within the context of our model, spatio-temporal heterogeneity in dynamics can be observed in tissues by analyzing the movement of individual cells. While the simulated time-dependent variations in the average mean-squared displacement is smooth, the movement of the individual cell is not (see Fig 3d). Cells move slowly and periodically undergo rapid 'jumps' or hops similar to the phenomenon in supercooled liquids [53, 54]. The squared displacement of individual cells (Fig 3d) vividly shows the heterogeneous behavior of different cells.

Polarized tumor growth. From our simulations, we constructed a spatial map of the velocities of the individual cells in the tumor. Using these maps, we characterized the spatial heterogeneity in the dynamics in order to elucidate regions of coordinated activity in the movement of cells. Fig. 4a shows a snapshot of the spatial map of the single cell velocities. The velocity map,

bioRxiv preprint doi: https://doi.org/10.1101/174599; this version posted August 10, 2017. The copyright holder for this preprint (which was not certified by peer review) is the author/funder, who has granted bioRxiv a license to display the preprint in perpetuity. It is made available under aCC-BY-NC-ND 4.0 International license.

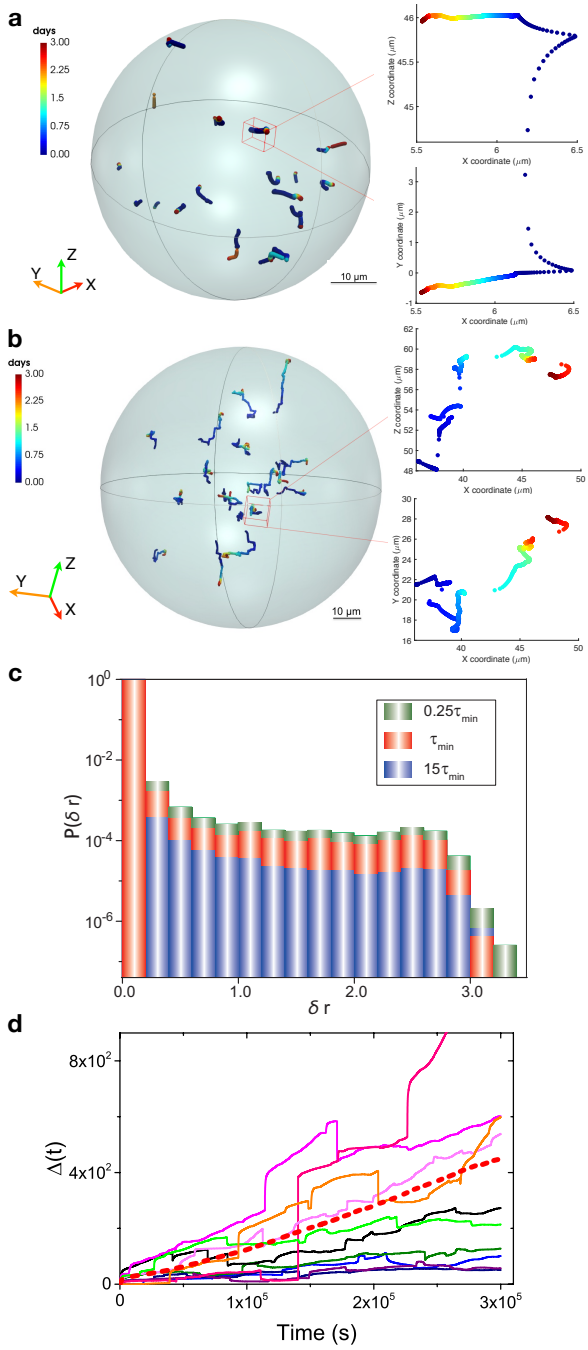

FIG. 3. **Spatial heterogeneity in tumor cell dynamics.** **a**, Trajectories (randomly chosen from the whole tumor) for slowly growing cells are shown. Cell cycle time is $15\tau_{min}$. Dynamic arrest due to caging in the glass-like phase is vividly illustrated. **b**, Trajectories for rapidly growing cells with cell cycle time $\tau = 0.25\tau_{min}$. Displacements of the cells are shown over 3 days representing the initial stages of tumor growth in **a** and **b**. Two representative trajectories (time dependence of the $x - z$ and $x - y$ coordinates) for the labelled cells are shown on the right of **a** and **b**. Length in **a** and **b** is measured in units of μm. The two colored spheres in **a** and **b** show the approximate extent of the tumor. **c**, Probability distribution of distance δr (in unit of μm), moved by cells over $\delta t = 100s$ for varying average cell cycle time τ. **d**, Time resolved squared displacements, $\Delta(t)$ (in unit of μm^2), of individual cells in a model for growing tumor ($\tau = \tau_{min}$). The average, shown as a dashed line for ≈ 800 such individual trajectories, is not relevant because of dynamic heterogeneity.

which spans more than eight orders of magnitude, reveals that there are cell-to-cell variations in the dynamics. More importantly, it also reveals the existence of spatial correlations between cell dynamics. In the tumor cross-section (Fig. 4b), faster moving cells are concentrated at the outer periphery of the tumor. By calculating the average magnitude of cell velocity as a function of radius, we show in Fig. 4c that faster moving cells are located at the outer periphery of the tumor quantitatively. Arrows indicating the velocity direction show that cells in the periphery tend to move farther away from the center of the tumor as opposed to cells closer to the center of the tumor whose direction of motion is essentially isotropic. This prediction agrees well with the experiments [32], which showed that cells at the periphery of the tumor spheroid move persistently along the radial direction, resulting in polarized tumor growth.

Mean angle θ between cell velocity and the position vector with respect to the center of the tumor plotted in Fig. 4d further illustrates that cell movement becomes persistently directed outward for cells closer to the outer layer of the tumor. The distribution of the θ angle at different distances (r) (see Fig. 4e) also illustrates that cell movement is isotropic close to the tumor center, while they move outward in a directed fashion (see the peak of the histogram in blue) at the periphery of the tumor. To quantify the heterogeneity in cell velocity, we plot the probability distribution of the velocity magnitude, $P(|v|)$, (Fig. 4f) accessible in experiments using direct imaging or particle image velocimetry methods [45, 46]. There is an abrupt change in the velocity distribution as a function of cell cycle time. At a longer cell cycle time, corresponding to the glass-like phase, $P(|v|)$ is sharply peaked at $|v| \approx 0$ and quickly decays for higher velocities. For the shorter cell cycle time, the velocity distribution is considerably broader. The peak of the distribution shifts to higher values corresponding to more invasive cells within the tumor.

Consistency with experiments. We show here that the minimal model captures the three critical aspects of a recent single-cell resolution experiment probing the invasion of cancer cells into a collagen matrix [32]: (i) Ensemble-averaged mean square displacement of individual cells exhibit a power-law behavior at long times ($\Delta(t) \sim t^{\alpha}$ with $\alpha \approx 1.4 \pm 0.04$ - see Fig. 2(a)) indicating that, on average, directed rather than random cell motion is observed. (ii) Cells exhibit a distinct topological motility profiles. At the spheroid periphery cell movement is persistently along the radial direction while stochastic movement is observed for cells closer to the center. Such spatial topological heterogeneity is well-described as arising in our model from pressure dependent inhibition (see Fig.3-4). (iii) The highly invasive spheroid boundary (deviating from what would be expected due to an isotropic random walk) as experimentally observed is qualitatively consistent with simulation results (see Fig. 14).

A salient feature of the dynamics of living cells is that

bioRxiv preprint doi: https://doi.org/10.1101/174599; this version posted August 10, 2017. The copyright holder for this preprint (which was not certified by peer review) is the author/funder, who has granted bioRxiv a license to display the preprint in perpetuity. It is made available under aCC-BY-NC-ND 4.0 International license.

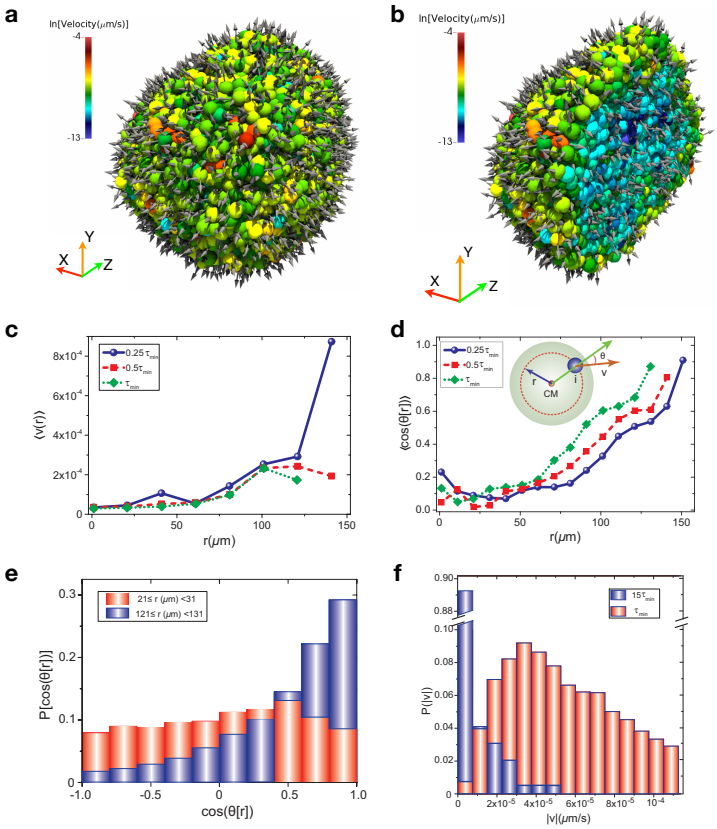

FIG. 4. **Heterogeneity in the tumor evolution.** **a**, Instantaneous snapshot of a collection $N \approx 1.3 \times 10^4$ cells at ≈ 3 days with $\tau = 0.25\tau_{min}$. Colors indicate the different velocities of the individual cells (in $\mu m/s$). **b**, Cross section through the clump of cells shown in Fig. 4a. Arrows denote the direction of velocity. **c**, Average speed of the cells as a function of the tumor radius at different τ. **d**, Mean angle θ (see the inset figure) between cell velocity and a line through the center of the tumor to the periphery as function of the tumor radius at different τ. **e**, Distribution of the angle (θ) at different distances (r) from tumor center at ≈ 3 days ($\tau = 0.25\tau_{min}$). **f**, Snapshot of the probability distribution of the velocity magnitude at two different cell cycle times at long time regime ($t > \tau$).

birth and death processes break number conservation, having consequences on their collective behavior [59]. To account for these processes leading to the super-diffusive behavior at long times, we establish a field theory based on stochastic quantization that account for the physical interactions of the cells as well as birth and death processes. Simulations and theory suggest a mechanism of the plausible universality in the onset of super-diffusive behavior in tumor growth and unrelated systems. Unexpectedly, the theory predicts the dynamics of invasion at all times that are in good agreement with recent experiments [32].

Onset of super-diffusion depends on cell division time. In previous works [25, 26], fluidization of tissues due to cell division and apoptosis was observed at the homeostatic state. Our work shows that a glass-to-fluid transition is driven by cell division at non-steady states and under free boundary conditions, relevant during early stages of cancer invasion. The transition from glass to fluid-like behavior is determined by the average cell division time. Super-diffusion in the mean-squared displacement due to highly polarized tumor growth is observed on a time scale corresponding to the cell division time with universal scaling exponent $\alpha \approx 1.3$.

CONCLUSIONS

Heterogeneity is a hallmark of cancer [60]. It is difficult to capture this characteristic of cancers in well-mixed models that exclude spatial information. An important signature of cell dynamic heterogeneity, large variations in the squared displacement of cells in the tumor, is observed. We find a broad velocity distribution among tumor cells driven by cell growth rate. The formation of spatial niches, with tumor periphery and center as distinct niches characterized by varying proliferative and cell signaling activities, alluded to as the driving factor behind intratumor heterogeneity (ITH) [61] is not well understood. Our model predicts the pressure dependent inhibition of cell growth to be the critical factor behind the development of distinct topological niches. Cells closer to the center of the tumor spheroid are surrounded by many other cells causing them to be predominantly in the dormant state and can move in random directions, while cells closer to the periphery can divide and move in a directed manner aiding tumor growth and invasiveness. We provide experimentally testable hypotheses on the signatures of heterogeneity: the onset of ITH could occur at very early stages of tumor growth (at the level of around 10,000 cells).

Besides the context of our work being rooted in understanding tumor growth, we expect our model to be relevant to the study of soft glassy materials. The motion of cells in our model is surprisingly consistent with the complex motion of bubbles in a foam, also shown to be super-diffusive [36] with the MSD exponent of $\alpha \approx 1.37 \pm 0.03$, consistent with both our theoretical predictions ($\alpha \approx 1.33$) and simulation results ($\alpha \approx 1.3$). The bubbles are characterized by birth death processes and pressure dependent growth, which we predict to be the driving factors behind super-diffusive behaviors observed in these diverse systems. An open question is how similar the Levy-type super-diffusion is in both systems. Emergence of underlying similarities in the motion of constituent particles between living systems such as cells and soft glassy materials such as foams suggest that many of the shared, but, as of yet unexplained dynamic behavior may emerge from a common underlying theme - birth death processes and pressure dependent growth inhibition.

bioRxiv preprint doi: https://doi.org/10.1101/174599; this version posted August 10, 2017. The copyright holder for this preprint (which was not certified by peer review) is the author/funder, who has granted bioRxiv a license to display the preprint in perpetuity. It is made available under aCC-BY-NC-ND 4.0 International license.

ACKNOWLEDGMENTS

We acknowledge Anne D. Bowen at the Visualization Laboratory (Vislab), Texas Advanced Computing Center for help with figure and movie visualizations. We are grateful to Mauro Mugnai, Naoto Hori and Upayan Baul for discussions and comments on the manuscript. This work is supported by the National Science Foundation (CHE 16-36424 and 16-32756). A. N. M and X. L. contributed equally to this work.

Appendix A: Theory

The behavior of the Mean Square Displacement ($\Delta(t)$), especially the time dependence of $\Delta(t)$ at intermediate and long times, can be theoretically obtained for the tumor growth model investigated using simulations. We consider the dynamics of a colony of cells in a dissipative environment with negligible inertial effects. The interaction between cells is governed by adhesion and excluded volume repulsion. The equation of motion for a single cell i is,

$$\frac{\partial \mathbf{r}_i}{\partial t} = -\sum_{j=1}^{N} \nabla U(\mathbf{r}_i(t) - \mathbf{r}_j(t)) + \eta_i(t), \tag{A1}$$

where U contains the following form of repulsive interactions with range λ, and favorable attractive interactions between cells with range σ,

$$U(\mathbf{r}(i) - \mathbf{r}(j)) = \frac{v}{(2\pi\lambda^2)^{3/2}} e^{-\frac{(\mathbf{r}(i)-\mathbf{r}(j))^2}{2\lambda^2}} - \frac{\kappa}{(2\pi\sigma^2)^{3/2}} e^{-\frac{(\mathbf{r}(i)-\mathbf{r}(j))^2}{2\sigma^2}}. \tag{A2}$$

v and κ above are the strengths of repulsive and attractive interactions respectively. The parameter κ mimics adhesion between cells. The noise (η_i in Eq. (A1)) is uncorrelated in time.

The simplified form for U, which captures minimally the interactions between cells but differs from the more elaborate model used in the simulations, allows us to obtain analytical results for $\Delta(t)$ vs t. In terms of the density field of a cell, $\phi_i(\mathbf{r}, t) = \delta[\mathbf{r} - \mathbf{r}_i(t)]$, a closed form Langevin equation for the density, $\phi(\mathbf{r}, t) = \sum_i \phi_i$ can be obtained using the approach introduced by Dean [62]. In order to study tumor cell dynamics, we extend the model phenomenologically to describe both cell division and death, and introduce a noise term that breaks the cell number conservation. These crucial features needed to describe tumor growth can be investigated using the Doi-Peliti (DP) formalism [63, 64], introduced in the context of reaction-diffusion processes. A related approach was used recently by Gelimson and Golestanian [65] to describe collective dynamics in a dividing colony of chemotactic cells.

We use a model to study the interplay between stochastic growth and apoptotic process, and use it to derive a

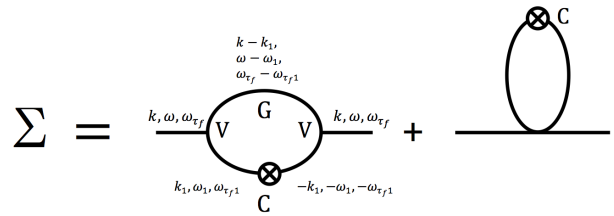

FIG. 5. The $\otimes$ is the noise correlations and the solid lines are the Green functions. The diagrams correspond to perturbation expansions in the theory (Eq. (A3)) in which the dynamical equations for the density field is expressed in fictitious time. Self-energy term (Σ) is obtained by contracting the two density ρ fields. The first diagram is the two loop contribution generated from the first order term (contains two ρ fields) in the equation for the density fields. The second diagram, with one loop contribution from the second order term (contains three ρ fields), resulting in the correction to $\omega^2 + \{C_0 k^2 U(\mathbf{k}) - (k_a - 2k_b C_0)\}^2$ does not have any new momentum dependance. Hence, only the first term is significant in producing the scaling results.
The vertex term is of the form: $V = \{i\omega + C_0 k^2 U(\mathbf{k}) - (k_a - 2k_b C_o)\}\{(-\mathbf{k_1} \cdot \mathbf{k})U(\mathbf{k_1}) - k_b\} + \{i\omega_1 + C_0 k_1^2 U(\mathbf{k_1}) - (k_a - 2k_b C_o)\}\{(-\mathbf{k_1} \cdot \mathbf{k})U(-\mathbf{k}) - k_b\} + \{i\omega_1 + C_0 k_1^2 U(\mathbf{k_1}) - (k_a - 2k_b C_o)\}\{(-\mathbf{k_1} \cdot (\mathbf{k} - \mathbf{k_1}))U(\mathbf{k} - \mathbf{k_1}) - k_b\}$. The Green function $G = i\omega_{\tau_f} + \frac{1}{2(k_a C_0 + k_b C_0^2)}[\omega^2 + \{C_0 k^2 U(\mathbf{k}) - (k_a - 2k_b C_0)\}^2]$ and the correlation function $C = GG^*$. The scaling of $\Delta(t)$ may be gleaned using the relation $C = (1/\omega_{\tau_f})\mathrm{Im}\, G$.

Langevin type equation for logistic growth. The birth reaction, $X \xrightarrow{k_a} X + X$, occurs with the rate constant k_a for each cell, and the backward reaction (apoptosis) $X + X \xrightarrow{k_b} X$ occurs with rate k_b. By incorporating birth and apoptosis, and assuming that the density fluctuates around a constant value, $\phi(\mathbf{r}, t) = C_0 + \rho(\mathbf{r}, t)$, we obtain the approximate equation for the density fluctuation, which in Fourier space reads,

$$\begin{aligned}\frac{\partial \rho(\mathbf{k}, t)}{\partial t} =& -C_0 k^2 U(\mathbf{k})\rho(\mathbf{k}, t) + (k_a - 2k_b C_0)\rho(\mathbf{k}, t) \\ &+ \int d\mathbf{q}(-\mathbf{q} \cdot \mathbf{k})U(\mathbf{q})\rho(\mathbf{q}, t)\rho(\mathbf{k} - \mathbf{q}, t) - k_b \int d\mathbf{q}\rho(\mathbf{q}, t)\rho(\mathbf{k} - \mathbf{q}) + \sqrt{k_a C_0 + k_b C_0^2} f_\phi.\end{aligned} \tag{A3}$$

We derived Eq. (A3) by expanding the density to lowest order in $\frac{\rho}{C_0}$ non-linearity. The noise f_ϕ satisfies

bioRxiv preprint doi: https://doi.org/10.1101/174599; this version posted August 10, 2017. The copyright holder for this preprint (which was not certified by peer review) is the author/funder, who has granted bioRxiv a license to display the preprint in perpetuity. It is made available under aCC-BY-NC-ND 4.0 International license.

$\langle f_\phi(\mathbf{r},t) f_\phi(\mathbf{r}',t')\rangle = \delta(\mathbf{r}-\mathbf{r}')\delta(t-t')$. In the hydrodynamic, $k \to 0$ and $t \to \infty$ limit, the first and third terms in the RHS of Eq. (A3) vanish, and hence the scaling behavior of $\Delta(t)$ at long times is determined solely by the death-birth terms.

The scaling of $\Delta(t)$ can be obtained by treating the non-linear terms in Eq. (A3) perturbatively using the Parisi-Wu stochastic quantization scheme [49, 66, 67], which is needed because Fluctuation Dissipation Theorem (FDT) is not satisfied in Eq. (A3) due to cell birth and death processes. In order to outline the essence of the theory, let us consider the probability distribution corresponding to the noise term given by

$$P(f_\phi) \propto \exp\left[-\int \frac{d^D\mathbf{k}}{(2\pi)^D}\frac{d\omega}{2\pi}\frac{1}{2} f_\phi(\mathbf{k},\omega) f_\phi(-\mathbf{k},-\omega)\right]. \tag{A4}$$

By re-expressing $P(f_\phi(\mathbf{k},\omega))$ in terms of $P(\rho(\mathbf{k},\omega))$, a Langevin equation of motion in the fictitious time, τ_f, may be derived in which FDT is satisfied. Consequently, in the $\tau_f \to \infty$ limit, the distribution function $P(\rho(\mathbf{k},\omega)) \propto \exp(-S(\mathbf{k},\omega))$, where $S(\mathbf{k},\omega)$ is derivable from Eqs. (A3) and (A4). Using this formalism, the Green's function can be obtained using perturbation theory by solving the Dyson equation,

$$[G]^{-1} = [G^{(0)}]^{-1} + \Sigma(\mathbf{k},\omega,\omega_{\tau_f}), \tag{A5}$$

where ω_{τ_f} is the frequency related to τ_f and $G_0^{-1} = i\omega_{\tau_f} + \frac{1}{2(k_aC_0+k_bC_0^2)}[\omega^2 + \{C_0k^2U(\mathbf{k}) - (k_a - 2k_bC_0)\}^2]$. After computing the self energy to second order in non-linearity, Eq. (A5) can be written as,

$$[G]^{-1}(\mathbf{k},\omega,\omega_{\tau_f}) = -i\omega_{\tau_f} + \frac{1}{2(D_0)}[\omega^2] + \frac{1}{2(\bar{D})}[\nu_{eff}^2 k^4], \tag{A6}$$

where $D_0 = k_aC_0 + k_bC_0^2$. The above equation allows us to determine an effective coefficient $\bar{D}$ from $G^{-1}(\mathbf{k},0,0)$,

$$\frac{1}{2(\bar{D})}[\nu_{eff}^2 k^4] = \frac{1}{2(D_0)}(\nu k^2)^2 + \Sigma(\mathbf{k},\omega,\omega_{\tau_f}), \tag{A7}$$

with $\nu = C_0U(\mathbf{k})$. In obtaining Eq. (A7), needed for calculating the scaling of $\Delta(t)$ in the intermediate time, the strength of the interactions are such that $C_0k^2U(\mathbf{k})$ dominates over $(k_a - 2k_bC_0)$. Expanding ν_{eff} about ν and $\bar{D}$ around D_0, and noting that the renormalization of ν dominates, we write using $\Delta\nu = \nu_{eff} - \nu$,

$$\Delta\nu k^2 = \frac{1}{2\nu k^2}\Sigma(\mathbf{k},\omega,\omega_{\tau_f}). \tag{A8}$$

In the spirit of self-consistent mode coupling theory, we now replace ν by $\Delta\nu$ in the self energy term $\Sigma(\mathbf{k},\omega,\omega_{\tau_f})$, use G as given by Eq. (A6), and the $C = GG^*$ correlation function, as follows from the FDT. According to scale transformation, $\omega \sim k^z$, $\omega_{\tau_f} \sim k^{2z}$, $G \sim k^{-2z}$, $C \sim k^{-4z}$ and the vertex factor $V \sim k^{z+2}$. The self energy term in Fig. (5) can be written as $\Sigma(\mathbf{k},\omega,\omega_{\tau_f}) \sim \int \frac{d^D\mathbf{k}'}{(2\pi)^D}\frac{d\omega'}{2\pi}\frac{d\omega'_{\tau_f}}{2\pi} VVGC$ (Fig. (5) provides a sketch of the calculations). By carrying out the momentum count of $\Sigma(\mathbf{k},\omega,\omega_{\tau_f})$, and noting that $\nu k^2 \sim k^z$, we find $\Sigma(k,\omega,\omega_{\tau_f}) \sim k^{D-z+4}$. Using Eq. (A8), we obtain $k^{z+2} \sim k^{D-z+4}$, leading to $z = 1 + \frac{D}{2}$.

Assuming dynamic scaling holds, the single cell mean-square displacement should behave as,

$$\Delta(t) =< [\mathbf{r}(t) - \mathbf{r}(0)]^2 >\sim t^{2/z} = t^\alpha. \tag{A9}$$

In 3D, $\alpha = \frac{4}{5} = 0.8$, implying $\Delta(t)$ should display sub-diffusive behavior. The theoretical prediction is in accord with the behavior of $\Delta(t)$ in the caging regime. In the long time limit, the non-linearity due to death-birth dominates over mechanical interactions ($\propto U(\mathbf{k})$). A similar procedure, as mentioned above, produces the dynamic exponent $z = D/2$. In this regime, $\alpha = 1.33$, implying super-diffusive motion, a prediction that is also in agreement with our simulations and experimental results [32]. Thus, the theory explains the simulation results, and by extension the experimental data, nearly quantitatively.

Appendix B: Multicellular Tumor Growth Model

We simulated the spatiotemporal dynamics of a multicellular tumor using a three dimensional (3D) agent-based model in which the cells in the tumor are represented as interacting objects. In this model, the cells grow stochastically as a function of time and divide upon reaching a critical size. The cell-to-cell interaction is characterized by direct elastic and adhesive forces. We also consider cell-to-cell and cell-to-matrix damping as a way of accounting for the effects of friction experienced by a moving cell due to other cells and by the extracellular matrix (ECM), respectively.

Each cell is modeled as a deformable sphere with a time dependent radius. Several physical properties such as the radius, elastic modulus, membrane receptor and ligand concentration, adhesive interaction, characterize each cell. Following previous studies [27, 28, 68], we use the Hertzian contact mechanics to model the magnitude of the elastic force between two spheres of radii R_i and R_j (Fig. 6a),

$$F_{ij}^{el} = \frac{h_{ij}^{3/2}(t)}{\frac{3}{4}\left(\frac{1-\nu_i^2}{E_i} + \frac{1-\nu_j^2}{E_j}\right)\sqrt{\frac{1}{R_i(t)} + \frac{1}{R_j(t)}}}, \tag{B1}$$

where E_i and ν_i, respectively, are the elastic modulus and Poisson ratio of cell i. The overlap between the spheres, if they interpenetrate without deformation, is h_{ij}, which is defined as $\max[0, R_i + R_j - |\vec{r}_i - \vec{r}_j|]$ with $|\vec{r}_i - \vec{r}_j|$ being the center-to-center distance between the two spheres (see Fig. 6a). The repulsive force in Eq. (B1) is valid for small virtual overlaps such that $h_{ij} << \min[R_i, R_j]$, and is likely to underestimate the actual repulsion between

bioRxiv preprint doi: https://doi.org/10.1101/174599; this version posted August 10, 2017. The copyright holder for this preprint (which was not certified by peer review) is the author/funder, who has granted bioRxiv a license to display the preprint in perpetuity. It is made available under aCC-BY-NC-ND 4.0 International license.

the cells [28]. Nevertheless, the model incorporates measurable mechanical properties of the cell, such as E_i and ν_i, and hence we use this form for the repulsive force.

Cell adhesion, mediated by receptors on the cell membrane, is the process by which cells interact and attach to one another. For simplicity, we assume that the receptor and ligand molecules are evenly distributed on the cell surface. Consequently, the magnitude of the adhesive force, F_{ij}^{ad}, between two cells i and j is expected to scale as a function of their contact area, A_{ij} [69]. We estimate F_{ij}^{ad} using [28],

$$F_{ij}^{ad} = A_{ij} f^{ad} \frac{1}{2}(c_i^{rec} c_j^{lig} + c_j^{rec} c_i^{lig}), \tag{B2}$$

where the c_i^{rec} (c_i^{lig}) is the receptor (ligand) concentration (assumed to be normalized with respect to the maximum receptor or ligand concentration so that $0 \leq c_i^{rec}, c_i^{lig} \leq 1$). The coupling constant f^{ad} allows us to rescale the adhesion force to account for the variabilities in the maximum densities of the receptor and ligand concentrations. We calculate the contact surface area, A_{ij}, using the Hertz model prediction, $A_{ij} = \pi h_{ij} R_i R_j/(R_i + R_j)$. The Hertz contact surface area is smaller than the proper spherical contact surface area. However, in dense tumors many spheres overlap, and thus the underestimation of the cell surface overlap may be advantageous in order to obtain a realistic value of the adhesion forces [28].

Repulsive and adhesive forces considered in Eqs.(B1) and (B2) act along the unit vector $\vec{n}_{ij}$ pointing from the center of cell j to the center of cell i (Fig. 6a). The force exerted by cell i on cell j, $\mathbf{F}_{ij}$, is shown in Fig. 6b. The total force on the ith cell is given by the sum over its nearest neighbors ($NN(i)$),

$$\vec{F}_i = \Sigma_{j\epsilon NN(i)}(F_{ij}^{el} - F_{ij}^{ad})\vec{n}_{ij}. \tag{B3}$$

We developed a distance sorting algorithm to efficiently provide a list of nearest neighbors in contact with the ith cell for use in the simulations. For any given cell, i, an array containing the distances from cell i to all the other cells is initially created. We then calculate, $R_i + R_j - |\vec{r}_i - \vec{r}_j|$ and sort the cells j satisfying $R_i + R_j - |\vec{r}_i - \vec{r}_j| > 0$ - a necessary condition for any cell j to be in contact with cell i.

Appendix C: Simulation Details

Equations of Motion: The spatial dynamics of the cell is computed based on the equation of motion [28, 70, 71] for a cell of mass m_i,

$$m_i \ddot{r}_i^{\alpha'} = F_i^{\alpha'}(t) - \Sigma_{\beta'} \gamma_i^{\alpha'\beta'} \dot{r}_i^{\beta'}(t) - \Sigma_{\beta'} \Sigma_j \gamma_{ij}^{\alpha'\beta'} [\dot{r}_i^{\beta'}(t) - \dot{r}_j^{\beta'}(t)], \tag{C1}$$

where the Greek indices $[\alpha', \beta'] = [x, y, z]$ are for coordinates, and the Latin indices $[i, j] = [1, 2, ..., N]$ are the cell indices. In Eq. (C1), $\gamma_i^{\alpha'\beta'}$ is the cell-to-medium friction coefficient, and $\gamma_{ij}^{\alpha'\beta'}$ is the cell-to-cell friction coefficient. The adhesive and repulsive forces are included in the term $F_i^{\alpha'}$. The cell-to-ECM friction coefficient is assumed to be given by the Stokes relation,

$$\gamma_i^{\alpha'\beta',visc} = 6\pi\eta R_i \delta^{\alpha'\beta'}, \tag{C2}$$

based on the friction of a sphere in a medium of viscosity η. Here, $\delta^{\alpha'\beta'}$ is the Kronecker delta.

As the Reynolds number for cells in a tissue is small [70], overdamped approximation is appropriate implying that the neglect of the inertial term $m_i \ddot{r}_i^{\alpha'} \approx 0$ is justified [28]. Since additional adhesive forces are also present, cell movement is further damped [72]. We simplify the equation of motion (Eq. (C1)), by replacing the intercellular drag term with a modified friction term, given that the movement of the bound cells is restricted. The modified friction term will contribute to the diagonal part of the damping matrix with $\gamma_i^{\alpha'\beta'} = \gamma_i^{\alpha'\beta',visc} + \gamma_i^{\alpha'\beta',ad}$ where,

$$\gamma_i^{\alpha'\beta',ad} = \gamma^{max} \Sigma_{j\epsilon NN(i)} (A_{ij} \frac{1}{2}(1 + \frac{\vec{F}_i \cdot \vec{n}_{ij}}{|\vec{F}_i|}) \times \frac{1}{2}(c_i^{rec} c_j^{lig} + c_j^{rec} c_i^{lig}))\delta^{\alpha'\beta'}. \tag{C3}$$

Notice that the added friction coefficient $\gamma_i^{\alpha'\beta',ad}$ is proportional to the cell-to-cell contact surface, implying that a cell in contact with many other cells would move less. The non-isotropic nature of the adhesive friction is evident from the factor $(1 + \frac{\vec{F}_i \cdot \vec{n}_{ij}}{|\vec{F}_i|})$ where the maximum contribution occurs when the net force $\vec{F}_i$ is parallel to a given unit vector, $\vec{n}_{ij}$, among the nearest neighbors. With these approximations, the equations of motion (Eq. (C1)) are now diagonal,

$$\dot{\vec{r}}_i = \frac{\vec{F}_i}{\gamma_i}. \tag{C4}$$

Effects of random forces: The neglect of random forces, which should be taken into account to satisfy the FDT, might seem like a drastic simplification. There are, however, two considerations. First, the tumor growth model involves birth and apoptosis. Hence, it behaves like an active system. Indeed, the theory outlined in Section A shows that under these conditions FDT is not satisfied, forcing us to adopt the stochastic quantization methods to compute response and correlation functions (Fig. (5)). Second, from practical considerations we note that the cellular diffusion constant is 10^{-4} μm^2/s or smaller [28], resulting in only small displacements for a large fraction of cells.

In order to verify that the contributions to the dynamics arising from the random noise is small, we modified Eq. (C4) to include the random forces,

$$\dot{\vec{r}}_i = \frac{\vec{F}_i}{\gamma_i} + \sqrt{2k_B T/\gamma_i^{visc}}\zeta_i(t), \tag{C5}$$

bioRxiv preprint doi: https://doi.org/10.1101/174599; this version posted August 10, 2017. The copyright holder for this preprint (which was not certified by peer review) is the author/funder, who has granted bioRxiv a license to display the preprint in perpetuity. It is made available under aCC-BY-NC-ND 4.0 International license.

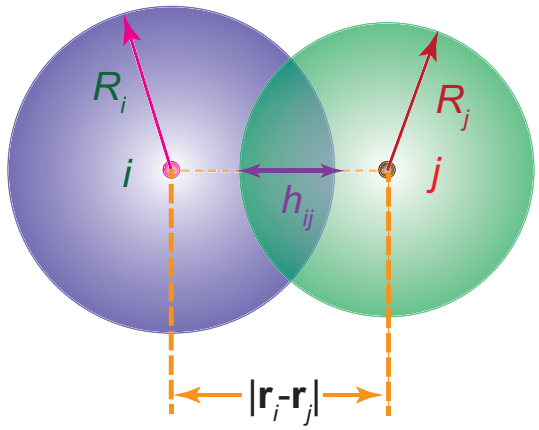

(a)

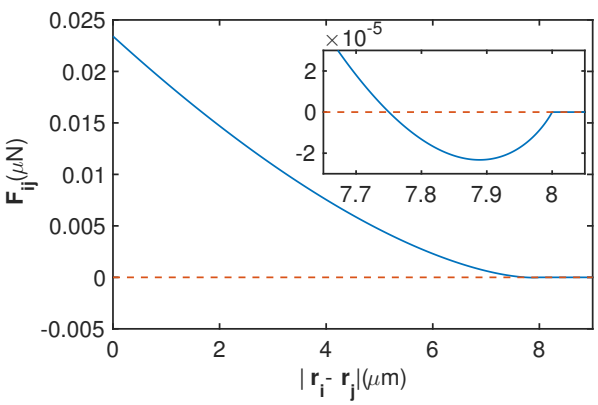

(b)

FIG. 6. **(a)** Illustration of two interpenetrating cells i and j with radii R_i and R_j, respectively. The distance between the centers of the two cells is $|\mathbf{r}_i - \mathbf{r}_j|$, and their overlap is h_{ij}. **(b)** Force on cell i due to j, $\mathbf{F}_{ij}$, for $R_i = R_j = 4\ \mu m$ using mean values of elastic modulus, poisson ratio, receptor and ligand concentration (see Table I). $\mathbf{F}_{ij}$ is plotted as a function of distance between the centers of the two cells. Inset shows the region where $\mathbf{F}_{ij}$ is attractive. When $|\mathbf{r}_i - \mathbf{r}_j| \geq R_i + R_j = 8\ \mu m$ the cells are no longer in contact, and hence, $\mathbf{F}_{ij} = 0$.

where k_B is the Boltzmann constant, T the temperature and ζ is white noise with zero mean and variance, $\langle \zeta_i(t)\zeta_i(t')\rangle = \delta(t-t')$. The corresponding diffusion constant, $k_B T/\gamma^{visc}$, is small. Thus, inclusion of random force has no consequence on the dynamics of tumor evolution. The results for $\Delta(t)$ as a function of t obtained using Eqs. (C4) and (C5) are identical (Fig. 7).

Cell Cycle: In our model, cells are in the dormant (D) or in the growth (G) phase. We track the sum of the normal pressure that a cell experiences due to contact with its neighbors, using,

$$p_i = \Sigma_{j\epsilon NN(i)} \frac{|\vec{F}_{ij} \cdot \vec{n}_{ij}|}{A_{ij}}. \tag{C6}$$

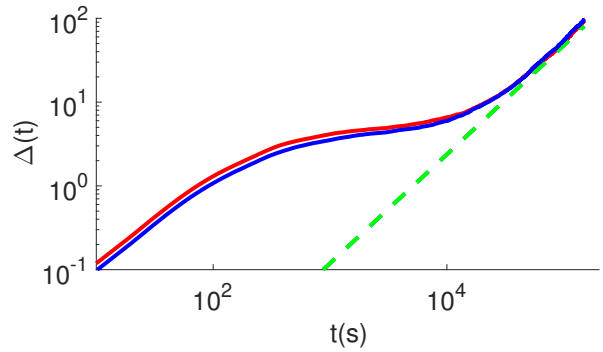

FIG. 7. Mean square displacement, $\Delta(t)$, with (blue) and without (red) random noise. The slope obtained from the long time limit are both 1.3 (dashed green). The two curves are almost identical, thus justifying the neglect of the random noise (second term in Eq. (C5)) in the simulations.

If the total pressure, p_i, exceeds a critical limit (p_c) the cell stops growing and enters the dormant phase (see the left panel in Fig. 8). For growing cells, their volume increases at a constant rate r_V. The cell radius is updated from a Gaussian distribution with the mean rate $\dot{R} = (4\pi R^2)^{-1} r_V$. Over the cell cycle time τ,

$$r_V = \frac{2\pi (R_m)^3}{3\tau}, \tag{C7}$$

where R_m is the mitotic radius. A cell divides once it grows to the fixed mitotic radius. To ensure volume conservation, upon cell division, we use $R_d = R_m 2^{-1/3}$ as the radius of the daughter cells (see the right panel in Fig. 8). The two resulting cells are placed at a center-to-center distance $d = 2R_m(1 - 2^{-1/3})$. The direction of the new cell location is chosen randomly from a uniform distribution on the unit sphere. One source of stochasticity in the cell movement in our model is due to random choice for the mitotic direction. Together with stochasticity in the cell cycle duration, we obtain fairly isotropic tumor spheroids.

Calibration of the model parameters: We compare the normalized volume of the growing tumor to experimental data [39], as a way of assessing if the parameters (Table I) used in our model are reasonable. The tumor volume, $V(t)$, normalized by the initial volume of the spheroid (V_0), was tracked experimentally using colon carcinoma cells [39] through experimental methods that are very different from the way we simulated tumor growth. The tumor growth was measured by imposing stress [39], known to inhibit cancer growth [73]. These effects are included in our model, which allows us to make quantitative comparisons between our simulations and experiments. The tumor volume is obtained in the simulation from, R_g, the radius of gyration,

$$R_g^2 = \frac{1}{N}\sum_i^N (\vec{r}_i - \vec{R}_{CM})^2, \tag{C8}$$

bioRxiv preprint doi: https://doi.org/10.1101/174599; this version posted August 10, 2017. The copyright holder for this preprint (which was not certified by peer review) is the author/funder, who has granted bioRxiv a license to display the preprint in perpetuity. It is made available under aCC-BY-NC-ND 4.0 International license.

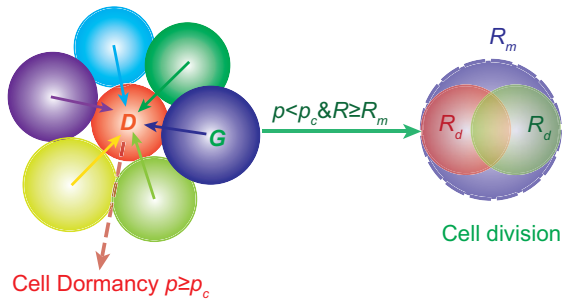

FIG. 8. Cell dormancy (left panel) and cell division (right panel). If the pressure p that a cell experiences (due to contacts with the neighboring cells) exceeds the critical pressure p_c, it enters the dormant state (D). Otherwise, the cells grow (G) until they reach the mitotic radius, R_m. At that stage, the mother cell divides into two identical daughter cells with the same radius R_d. We assume that the total volume upon cell division is conserved.

where $\vec{R}_{CM} = (1/N)\Sigma_i \vec{r}_i$ is the tumor center of mass and N the total number of cells. The volume $V(t)$ is given by $(4\pi/3)R_g^3(t)$. Our simulation of the growth of the spheroid tumor volume in the early stages is in good agreement with experimental data (see Fig. 9a). Thus, our model captures quantitative aspects of tumor growth.

In the experiment [39], $V(t)/V_0$ was measured for external pressure ranging from $0 - 20$kPa. In Fig. (9a), we compared our simulation results with the 500Pa result from experiments [39]. This is rationalized as follows. Unlike in experiments, the pressure is internally generated as the tumor grows (Fig. 9b) with a distribution that changes with time. The mean value of the pressure (see dashed lines in Fig. 9b) at the longest time is ≈ 100Pa. Thus, it is most appropriate to compare our results obtained using $p_c = 100$Pa with experiments in which external pressure is set at 500Pa.

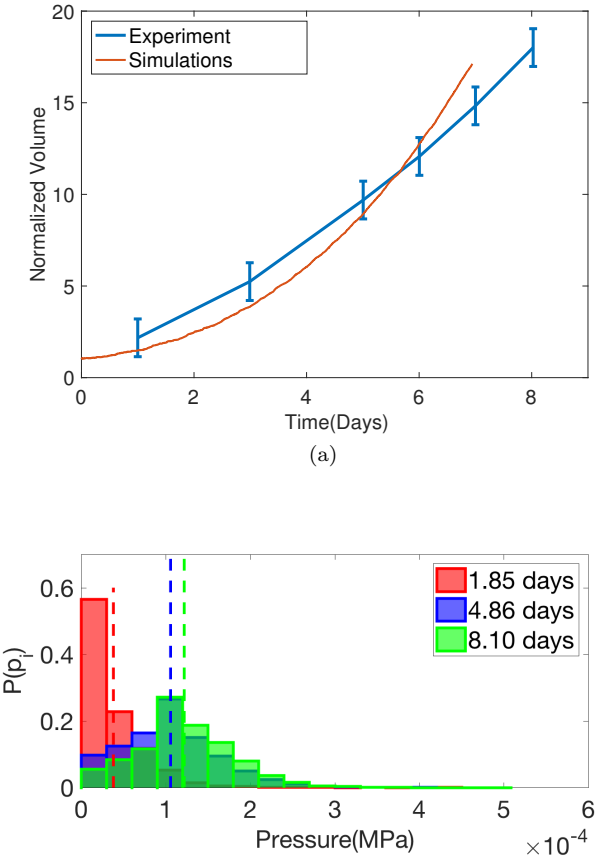

FIG. 9. **(a)** Normalized volume, $V(t)/V_0$, of a tumor spheroid as a function of time. The result of simulation (red) agrees quantitatively with experimental data obtained for the tumor spheroid growth at an applied pressure of 500Pa [39]. We used a critical pressure $p_c = 100$Pa and cell division time of $\tau = \tau_{min}$ in the simulations. The reason for comparing the results from the $p_c = 100$Pa simulations with the growth dynamics obtained in the colon carcinoma cells with an external pressure of 500Pa is explained in the Appendix text. **(b)** Distribution of pressure as a function of total growth time with cell division time $\tau = \tau_{min}$. The mean values are indicated by dashed lines.

Appendix D: Data Analyses

Pair correlation functions: In order to assess the spatial variation in the positions of the cells as the tumor grows, we calculated the pair correlation function using,

$$g(r) = \frac{V}{4\pi r^2 N^2} \sum_i^N \sum_{j \neq i}^N \delta(r - |\vec{r}_i - \vec{r}_j|). \qquad \text{(D1)}$$

The pair correlation function at different cell cycle times (τ) is shown in Fig. 10. At longer cell cycle times, $g(r)$ clearly illustrates that the cells in the system are packed more closely. The system transits from a liquid-like to a glass-like structure as τ is increased, as indicated by the peaks in $g(r)$.

Influence of cell adhesion strength on self-intermediate scattering function $F_s(q,t)$: Most of our results are obtained using a fixed value for the cell adhesion strength $f^{ad} = 10^{-4}\mu\text{N}/\mu\text{m}^2$ (see Table I). However, during tumor progression cell adhesion strength could vary [74]. To check the influence of this variation, we calculated the self-intermediate scattering functions $F_s(q,t)$ (see the main text for definition) for different values of f^{ad} (see Fig. 11). Compared to Fig. 2(b) in the Main text, the time scale associated with the first relaxation process corresponding to cell movement within the cage is slower as f^{ad} increases. Cells are trapped by their neighbors in this time regime making it more difficult for cells to move within the cage as f^{ad} increases, leading to an increase in the relaxation time. The relaxation time dependence on the values of f^{ad} is weaker for the sec-

bioRxiv preprint doi: https://doi.org/10.1101/174599; this version posted August 10, 2017. The copyright holder for this preprint (which was not certified by peer review) is the author/funder, who has granted bioRxiv a license to display the preprint in perpetuity. It is made available under aCC-BY-NC-ND 4.0 International license.

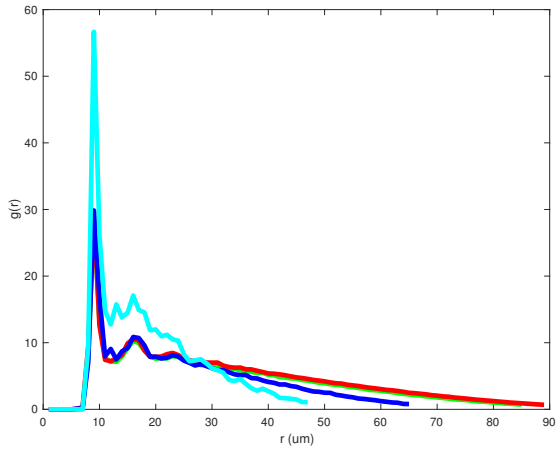

FIG. 10. Pair correlation function at four different cell division times (τ): $0.2\tau_{min}$ (red), $0.5\tau_{min}$ (green), τ_{min} (blue), and $10\tau_{min}$ (cyan). The cells are packed more closely at longer cell cycle times as reflected by the sharper peak for the cyan line compared to the others. The distance, r, at which $g(r)$ approaches zero is considerably smaller for $\tau = 10\tau_{min}$. The distance at which the first peak appears is $\approx 2R_m \approx 10\mu m$ (Table I), which implies that despite being soft the cells in the interior are densely packed, as in a body centered cubic lattice.

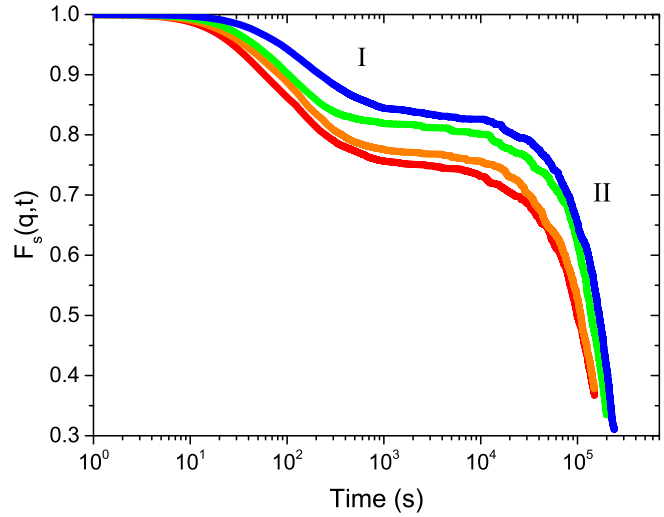

FIG. 11. The self-intermediate scattering function, $F_s(q,t)$, at different values of f^{ad}. From left to right, the f^{ad} values are, 5×10^{-5} (red), 10^{-4} (orange), 2×10^{-4} (green), $3 \times 10^{-4} \mu N/\mu m^2$ (blue) respectively. The first relaxation process depends on the strength of f^{ad} while the second relaxation process is not significantly affected by f^{ad}, as seen from the partial overlap in $F_s(q,t)$, at long times.

ond process corresponding to transitions out of the cage. This finding is in agreement with our theoretical prediction that in the long time regime, the dynamics of cell migration is determined by birth and death processes, and is impervious to the details of interactions between the cells. As a consequence there is a universal power law dependence of the mean square displacement (Eq. A9).

The scaling behavior of the MSD at early times: In the main text, we mainly focused on the MSD, $\Delta(t)$, at intermediate and long times. The behavior of $\Delta(t)$ in these time regimes is independent of the initial conditions (see Inset of Fig. 12). The scaling of MSD at early times is likely to be influenced by the initial condition of the tumor, and by implication the rate of metastasis. From the perspective of disease propagation, the initial stages are likely to be the most important. We started our simulation, at $t = 0$, by placing a collection of cells confined to a cubic box at random positions. At all later times, $t > 0$, we use free boundary conditions. We study the effect of varying the initial ($t = 0$) density of the seed cancer cells on the rate of tumor growth at early times. The cells are packed more closely as the size of the box at $t = 0$ decreases, and are separated far away from one another for a larger box. Fig. 12 shows $\Delta(t)$ at early times ($t < 10^3 s << \tau_{min}$) in a log-log scale for three different initial conditions: 100 cells packed in a cubic box with volume 8000 (blue), 64,000 (red), and 10^6 (orange) μm^3 respectively. At early times $\Delta(t)$ can be fit to a power-law ($\Delta(t) \propto t^\alpha$). The scaling exponent α increases as the initial tumor density increases (see Fig. 12). This behavior is expected as closer packing results in stronger repulsion, leading to faster cell mobility at early times. This observation suggests that the size of the confinement of the initial tumor plays an important role in cell movement at early times. The microenvironment might dictate the size of the region to which the initial tumor is localized. In other words, initial low density tumors are likely to be less virulent compared to high density tumors.

van-Hove Function: Probability distribution, $P(\delta r)$, of multi time step cell displacement was shown in Fig. 3c (see Main text) for different values of the cell cycle time. To analyze the displacement distribution, we fit the van-Hove function at normal cell division time (τ_{min}) to a Gaussian distribution, which is the expected behavior for isotropic diffusive motion. However, for the movement of cancer cells, the distribution $P(\delta r)$ is decidedly non-Gaussian, as evidenced by the fat-tail in $P(\delta r)$ (Fig. 13). The probability of large displacements, above $1.3\mu m$, is much larger than what would be expected from a Gaussian distribution.

Average Velocity and Cell Velocity Polarization: We calculate the average velocity of cells at different radii of the tumor using,

$$\langle v(r) \rangle = \frac{\Sigma_i v_i \delta(r - (|\vec{R}_{CM} - \vec{r}_i|))}{\Sigma_i \delta(r - (|\vec{R}_{CM} - \vec{r}_i|))}. \qquad \text{(D2)}$$

To calculate the radius-dependent average polarization in cell velocity, we first define a vector pointing from the center of mass of the tumor to the cell position $\vec{c}_i = \vec{r}_i - \vec{R}_{CM}$ (see the green arrow in the inset of Fig. 4d).

bioRxiv preprint doi: https://doi.org/10.1101/174599; this version posted August 10, 2017. The copyright holder for this preprint (which was not certified by peer review) is the author/funder, who has granted bioRxiv a license to display the preprint in perpetuity. It is made available under aCC-BY-NC-ND 4.0 International license.

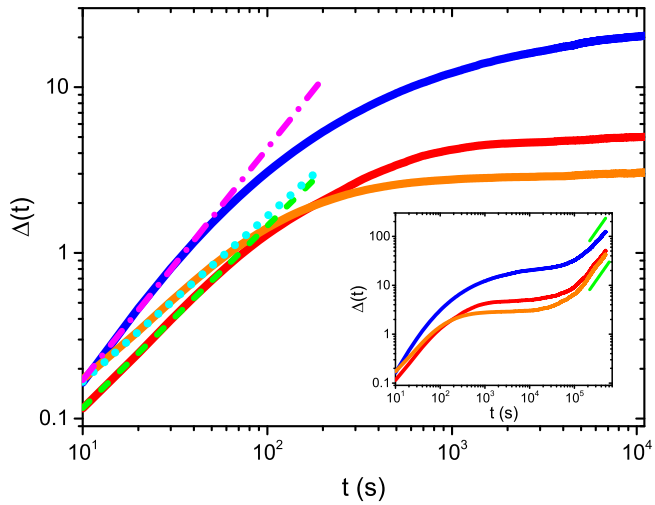

FIG. 12. Mean squared displacement, $\Delta(t)$, in units of μm^2 for different initial conditions. At $t = 0$, 100 cells are randomly placed in a volume of 8000 (blue), 64,000 (red), and 10^6 (orange) μm^3. The slope of the three lines is 1.4 (purple), 1.1 (dashed green), and 1.0 (cyan), respectively at early times. In the inset, the slopes obtained from the long time limit are all 1.3 (solid green) irrespective of the initial condition. The higher exponent for tumors that are denser initially might be relevant for the virulency of cancers.

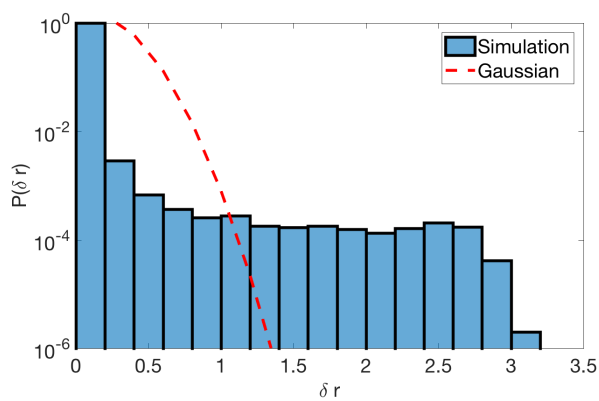

FIG. 13. The probability distribution $P(\delta r)$ of cell displacements ($|\delta r| = |r(t+100) - r(t)|$ in units of μm) over $t = 100s$ is shown. The histogram was constructed by analyzing $\approx 10^6$ displacements. For comparison purposes, a Gaussian distribution fit is shown (dashed line). The striking non-Gaussian behavior, with fat tails, is one indication of heterogeneity.

The angle θ (see the inset of Fig. 4d) between each cell velocity (orange arrow) and the the vector (green arrow) from the center of mass to the tumor periphery can be calculated from $\cos(\theta)_i = \vec{c}_i \cdot \vec{v}_i / (|\vec{c}_i||\vec{v}_i|)$. The average of this angle as a function of radius is calculated using,

$$\langle \cos(\theta[r]) \rangle = \frac{\Sigma_i \cos(\theta[r])_i \delta(r - (|\vec{R}_{CM} - \vec{r}_i|))}{\Sigma_i \delta(r - (|\vec{R}_{CM} - \vec{r}_i|))}. \quad \text{(D3)}$$

The results are presented in Fig. 4d in the main text.

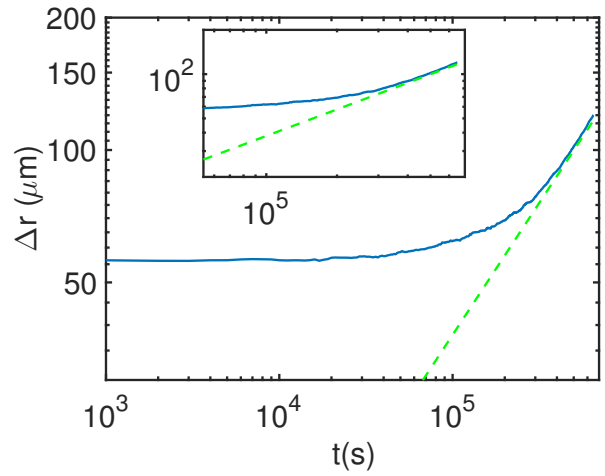

FIG. 14. The invasion distance, $\Delta r(t)$ (Eq. D4), as a function of time. The exponent of the invasion distance, as indicated by the dashed green line, determined using $\Delta r \propto t^{\xi}$ is $\xi \approx 0.6$. Note that this value and the one extracted from experiments [32] are in reasonable agreement. The inset shows $\Delta r(t)$ for $\tau > \tau_{min}$.

Tumor invasion distance: The invasion or spreading distance (see Fig. 14) of the growing tumor, $\Delta r(t)$, is determined by measuring the average distance from the tumor center of mass (R_{CM}) to the cells at the tumor periphery,

$$\Delta r(t) = \frac{1}{N_b} \sum_i^{N_b} |\vec{r}_i - \vec{R}_{CM}|, \quad \text{(D4)}$$

where the sum i is over N_b, the number of cells at the tumor periphery.

In order to find the cells at the tumor periphery (N_b), we denote the collection of all cells N as a set of vertices $\{1, 2, 3.....N\}$ in $\mathbb{R}^3$ where the vertices represent the center point of each cell. We generate a 3D structure of tetrahedrons using these vertices, where each tetrahedron is comprised of 4 vertices. Let T be the total number of tetrahedrons. Since each tetrahedron has 4 faces, the total number of faces is $4T$. Any face that is not on the boundary of the 3D structure is shared by 2 tetrahedrons but the boundary faces are not shared. Thus, our aim is to find the set of unshared boundary faces out of the total number, $4T$, of faces. Once the boundary faces are obtained, we know the list of vertices, and hence the positions of cells at the tumor periphery, allowing us to compute $\Delta r(t)$ in Eq. (D4).

The dependence of $\Delta r(t)$ on t in Fig. 14 shows that for $t \leq \tau_{min}$, the invasion radius is roughly constant, which is expected. As cells divide the tumor invasion distance, $\Delta r(t)$, increases as t^{ξ} with $\xi \sim 0.6$ for $t > \tau_{min}$, a value that is not inconsistent with experiments [32].

bioRxiv preprint doi: https://doi.org/10.1101/174599; this version posted August 10, 2017. The copyright holder for this preprint (which was not certified by peer review) is the author/funder, who has granted bioRxiv a license to display the preprint in perpetuity. It is made available under aCC-BY-NC-ND 4.0 International license.

Appendix E: MOVIES

In order to visualize the dynamic growth of the tumor we generated movies from the simulation. They demonstrate vividly the polarized growth of the tumor, which we have quantified using various measures.

Supplementary Movie 1. 3D growth of tumor

This movies shows the three dimensional growth of the tumor over ≈ 8 days. Each frame is at 1000 seconds. The cell cycle time $\tau = \tau_{min}$. Colormap indicates the life time of the cells. Newborn cells are shown in blue and older cells that have lived longer in red (color bar in video shows cell lifetime in seconds). Cell division and death events are explicitly depicted.

Supplementary Movie 2. Cross section view through the growing tumor spheroid

Illustration of an alternate view of the growing tumor shown in Supplementary Movie 1. Cells with longer lifetimes are mostly localized to the center of the tumor with some of them moving to the periphery. Newly born cells are mostly located in the periphery and division events are amplified in the periphery compared to the center of the tumor. Color bar shows cell lifetime.

Supplementary Movie 3. Moving clip through a tumor showing velocity heterogeneity

This video visualizes the velocity heterogeneity within the tumor. Colormap indicates the speed of cells (shown in log scale) and the direction of velocity is indicated by an arrow. The video begins with a snapshot of the tumor after ≈ 3 days of growth at $\tau = 0.25\tau_{min}$. A clip moving through the tumor shows the velocity distribution of cells over different slices. It can be vividly seen that cells move slowly closer to the center while faster moving cells are mostly in the periphery. Direction of velocity is more randomly oriented in the tumor center but is mostly polarized outward approaching the periphery.

Table I: The parameters used in the simulation.

Parameters	**Values**	**References**
Timestep (Δt)	1s - 10s	This paper
Critical Radius for Division (R_m)	5 μm	[28]
Extracellular Matrix (ECM) Viscosity (η)	0.005 kg/(μm s)	[75]
Benchmark Cell Cycle Time (τ_{min})	54000 s	[76–78]
Adhesive Coefficient (f^{ad})	$10^{-4}\mu$N/μm^2	[28]
Mean Cell Elastic Modulus (E_i)	10^{-3}MPa	[75]
Mean Cell Poisson Ratio (ν_i)	0.5	[28]
Death Rate (b)	10^{-6}s^{-1}	This paper
Mean Receptor Concentration (c^{rec})	1.0 (Normalized)	[28]
Mean Ligand Concentration (c^{lig})	1.0 (Normalized)	[28]
Adhesive Friction γ^{max}	10^{-4}kg/(μm^2 s)	This paper
Threshold Pressue (p_c)	10^{-4}MPa	[28, 39]

[1] B. Barres, I. Hart, H. Coles, J. Burne, J. Voyvodic, W. Richardson, and M. Raff, "Cell death and control of cell survival in the oligodendrocyte lineage," *Cell*, vol. 70, no. 1, pp. 31–46, 1992.

[2] R. Weinberg, *The biology of cancer*. Garland science, 2013.

[3] D. Ingber, "Mechanobiology and diseases of mechanotransduction," *Ann Med*, vol. 35, no. 8, pp. 564–577, 2003.

[4] F. Guilak, D. M. Cohen, B. T. Estes, J. M. Gimble, W. Liedtke, and C. S. Chen, "Control of stem cell fate by physical interactions with the extracellular matrix," *Cell stem cell*, vol. 5, no. 1, pp. 17–26, 2009.

[5] S. Kumar and V. M. Weaver, "Mechanics, malignancy, and metastasis: the force journey of a tumor cell," *Cancer Metastasis Rev*, vol. 28, no. 1, pp. 113–127, 2009.

[6] W. G. Stetler-Stevenson, S. Aznavoorian, and L. A. Liotta, "Tumor cell interactions with the extracellular matrix during invasion and metastasis," *Annu Rev Cell Biol*, vol. 9, no. 1, pp. 541–573, 1993.

[7] D. T. Tambe, C. C. Hardin, T. E. Angelini, K. Rajendran, C. Y. Park, X. Serra-Picamal, E. H. Zhou, M. H. Zaman, J. P. Butler, D. A. Weitz, *et al.*, "Collective cell guidance by cooperative intercellular forces," *Nature materials*, vol. 10, no. 6, p. 469, 2011.

[8] M. C. Marchetti, J. Joanny, S. Ramaswamy, T. Liverpool, J. Prost, M. Rao, and R. A. Simha, "Hydrodynamics of soft active matter," *Reviews of Modern Physics*, vol. 85, no. 3, p. 1143, 2013.

[9] T. E. Angelini, E. Hannezo, X. Trepat, M. Marquez, J. J. Fredberg, and D. A. Weitz, "Glass-like dynamics of collective cell migration," *Proc Natl Acad Sci USA*, vol. 108, no. 12, pp. 4714–4719, 2011.

[10] M. Sadati, N. T. Qazvini, R. Krishnan, C. Y. Park, and J. J. Fredberg, "Collective migration and cell jamming," *Differentiation*, vol. 86, no. 3, pp. 121–125, 2013.

[11] T. E. Angelini, E. Hannezo, X. Trepat, J. J. Fredberg, and D. A. Weitz, "Cell migration driven by cooperative substrate deformation patterns," *Physical review letters*, vol. 104, no. 16, p. 168104, 2010.

[12] E.-M. Schoetz, M. Lanio, J. A. Talbot, and M. L. Manning, "Glassy dynamics in three-dimensional embryonic tissues," *J R Soc Interface*, vol. 10, no. 89, p. 20130726, 2013.

bioRxiv preprint doi: https://doi.org/10.1101/174599; this version posted August 10, 2017. The copyright holder for this preprint (which was not certified by peer review) is the author/funder, who has granted bioRxiv a license to display the preprint in perpetuity. It is made available under aCC-BY-NC-ND 4.0 International license.

[13] I. González-García, R. V. Solé, and J. Costa, "Metapopulation dynamics and spatial heterogeneity in cancer," *Proceedings of the National Academy of Sciences*, vol. 99, no. 20, pp. 13085–13089, 2002.

[14] R. Durrett and S. A. Levin, "Stochastic spatial models: a user's guide to ecological applications," *Philosophical Transactions of the Royal Society of London B: Biological Sciences*, vol. 343, no. 1305, pp. 329–350, 1994.

[15] T. Nagai and H. Honda, "A dynamic cell model for the formation of epithelial tissues," *Philosophical Magazine B*, vol. 81, no. 7, pp. 699–719, 2001.

[16] D. Bi, X. Yang, M. C. Marchetti, and M. L. Manning, "Motility-driven glass and jamming transitions in biological tissues," *Phys Rev X*, vol. 6, no. 2, p. 021011, 2016.

[17] B. Li and S. X. Sun, "Coherent motions in confluent cell monolayer sheets," *Biophysical journal*, vol. 107, no. 7, pp. 1532–1541, 2014.

[18] A. G. Fletcher, M. Osterfield, R. E. Baker, and S. Y. Shvartsman, "Vertex models of epithelial morphogenesis," *Biophysical journal*, vol. 106, no. 11, pp. 2291–2304, 2014.

[19] T. J. Newman, "Modeling multi-cellular systems using sub-cellular elements," *Mathematical Biosciences and Engineering: MBE*, vol. 2, no. 3, pp. 613–624, 2005.

[20] F. Graner and J. A. Glazier, "Simulation of biological cell sorting using a two-dimensional extended potts model," *Physical review letters*, vol. 69, no. 13, p. 2013, 1992.

[21] A. Szabó, R. Ünnep, E. Méhes, W. Twal, W. Argraves, Y. Cao, and A. Czirók, "Collective cell motion in endothelial monolayers," *Physical biology*, vol. 7, no. 4, p. 046007, 2010.

[22] B. A. Camley, Y. Zhang, Y. Zhao, B. Li, E. Ben-Jacob, H. Levine, and W.-J. Rappel, "Polarity mechanisms such as contact inhibition of locomotion regulate persistent rotational motion of mammalian cells on micropatterns," *Proceedings of the National Academy of Sciences*, vol. 111, no. 41, pp. 14770–14775, 2014.

[23] B. A. Camley and W.-J. Rappel, "Physical models of collective cell motility: from cell to tissue," *Journal of Physics D: Applied Physics*, vol. 50, no. 11, p. 113002, 2017.

[24] S. Hilgenfeldt, S. Erisken, and R. W. Carthew, "Physical modeling of cell geometric order in an epithelial tissue," *Proceedings of the National Academy of Sciences*, vol. 105, no. 3, pp. 907–911, 2008.

[25] J. Ranft, M. Basan, J. Elgeti, J.-F. Joanny, J. Prost, and F. Jülicher, "Fluidization of tissues by cell division and apoptosis," *Proc Natl Acad Sci USA*, vol. 107, no. 49, pp. 20863–20868, 2010.

[26] D. Matoz-Fernandez, K. Martens, R. Sknepnek, J. Barrat, and S. Henkes, "Cell division and death inhibit glassy behaviour of confluent tissues," *Soft Matter*, vol. 13, no. 17, pp. 3205–3212, 2017.

[27] D. Drasdo and S. Höhme, "A single-cell-based model of tumor growth in vitro: monolayers and spheroids," *Phys Biol*, vol. 2, no. 3, p. 133, 2005.

[28] G. Schaller and M. Meyer-Hermann, "Multicellular tumor spheroid in an off-lattice voronoi-delaunay cell model," *Phys Rev E*, vol. 71, no. 5, p. 051910, 2005.

[29] P.-H. Wu, A. Giri, S. X. Sun, and D. Wirtz, "Three-dimensional cell migration does not follow a random walk," *Proceedings of the National Academy of Sciences*, vol. 111, no. 11, pp. 3949–3954, 2014.

[30] N. Gal and D. Weihs, "Intracellular mechanics and activity of breast cancer cells correlate with metastatic potential," *Cell biochemistry and biophysics*, vol. 63, no. 3, pp. 199–209, 2012.

[31] P. Dieterich, R. Klages, R. Preuss, and A. Schwab, "Anomalous dynamics of cell migration," *Proceedings of the National Academy of Sciences*, vol. 105, no. 2, pp. 459–463, 2008.

[32] A. M. J. Valencia, P.-H. Wu, O. N. Yogurtcu, P. Rao, J. DiGiacomo, I. Godet, L. He, M.-H. Lee, D. Gilkes, S. X. Sun, *et al.*, "Collective cancer cell invasion induced by coordinated contractile stresses," *Oncotarget*, vol. 6, no. 41, p. 43438, 2015.

[33] M. Pickl and C. Ries, "Comparison of 3d and 2d tumor models reveals enhanced her2 activation in 3d associated with an increased response to trastuzumab," *Oncogene*, vol. 28, no. 3, pp. 461–468, 2009.

[34] K. Wolf, Y. I. Wu, Y. Liu, J. Geiger, E. Tam, C. Overall, M. S. Stack, and P. Friedl, "Multi-step pericellular proteolysis controls the transition from individual to collective cancer cell invasion," *Nat Cell Biol*, vol. 9, no. 8, pp. 893–904, 2007.

[35] A. Gopal and D. Durian, "Relaxing in foam," *Physical review letters*, vol. 91, no. 18, p. 188303, 2003.

[36] H. J. Hwang, R. A. Riggleman, and J. C. Crocker, "Understanding soft glassy materials using an energy landscape approach," *Nat Mater*, vol. 15, no. 9, pp. 1031–1036, 2016.

[37] D. F. Quail and J. A. Joyce, "Microenvironmental regulation of tumor progression and metastasis," *Nat Med*, vol. 19, no. 11, pp. 1423–1437, 2013.

[38] R. K. Jain, J. D. Martin, and T. Stylianopoulos, "The role of mechanical forces in tumor growth and therapy," *Annu Rev Biomed Eng*, vol. 16, pp. 321–346, 2014.

[39] F. Montel, M. Delarue, J. Elgeti, L. Malaquin, M. Basan, T. Risler, B. Cabane, D. Vignjevic, J. Prost, G. Cappello, *et al.*, "Stress clamp experiments on multicellular tumor spheroids," *Phys Rev Lett*, vol. 107, no. 18, p. 188102, 2011.

[40] A. D. Conger and M. C. Ziskin, "Growth of mammalian multicellular tumor spheroids," *Cancer Res*, vol. 43, no. 2, pp. 556–560, 1983.

[41] E. Mandonnet, J.-Y. Delattre, M.-L. Tanguy, K. R. Swanson, A. F. Carpentier, H. Duffau, P. Cornu, R. Van Effenterre, E. C. Alvord, and L. Capelle, "Continuous growth of mean tumor diameter in a subset of grade ii gliomas," *Ann Neurol*, vol. 53, no. 4, pp. 524–528, 2003.

[42] M. Simeoni, P. Magni, C. Cammia, G. De Nicolao, V. Croci, E. Pesenti, M. Germani, I. Poggesi, and M. Rocchetti, "Predictive pharmacokinetic-pharmacodynamic modeling of tumor growth kinetics in xenograft models after administration of anticancer agents," *Cancer Res*, vol. 64, no. 3, pp. 1094–1101, 2004.

[43] D. Hart, E. Shochat, and Z. Agur, "The growth law of primary breast cancer as inferred from mammography screening trials data," *Br J Cancer*, vol. 78, no. 3, pp. 382–387, 1998.

[44] D. R. Grimes, P. Kannan, A. McIntyre, A. Kavanagh, A. Siddiky, S. Wigfield, A. Harris, and M. Partridge, "The role of oxygen in avascular tumor growth," *PloS one*, vol. 11, no. 4, p. e0153692, 2016.

[45] F. Pampaloni, E. G. Reynaud, and E. H. Stelzer, "The third dimension bridges the gap between cell culture and live tissue," *Nat Rev Mol Cell Biol*, vol. 8, no. 10, pp. 839–845, 2007.

bioRxiv preprint doi: https://doi.org/10.1101/174599; this version posted August 10, 2017. The copyright holder for this preprint (which was not certified by peer review) is the author/funder, who has granted bioRxiv a license to display the preprint in perpetuity. It is made available under aCC-BY-NC-ND 4.0 International license.

[46] K. Alessandri, B. R. Sarangi, V. V. Gurchenkov, B. Sinha, T. R. Kießling, L. Fetler, F. Rico, S. Scheuring, C. Lamaze, A. Simon, *et al.*, "Cellular capsules as a tool for multicellular spheroid production and for investigating the mechanics of tumor progression in vitro," *Proc Natl Acad Sci USA*, vol. 110, no. 37, pp. 14843–14848, 2013.

[47] E. R. Weeks, J. C. Crocker, A. C. Levitt, A. Schofield, and D. A. Weitz, "Three-dimensional direct imaging of structural relaxation near the colloidal glass transition," *Science*, vol. 287, no. 5453, pp. 627–631, 2000.

[48] W. K. Kegel and A. van Blaaderen, "Direct observation of dynamical heterogeneities in colloidal hard-sphere suspensions," *Science*, vol. 287, no. 5451, pp. 290–293, 2000.

[49] G. Parisi and Y. S. Wu, "Perturbation theory without gauge fixing," *Sci Sin*, vol. 24, no. 4, pp. 483–469, 1981.

[50] T. Kirkpatrick, D. Thirumalai, and P. G. Wolynes, "Scaling concepts for the dynamics of viscous liquids near an ideal glassy state," *Physical Review A*, vol. 40, no. 2, p. 1045, 1989.

[51] L. Berthier, G. Biroli, J.-P. Bouchaud, L. Cipelletti, and W. van Saarloos, *Dynamical heterogeneities in glasses, colloids, and granular media*, vol. 150. OUP Oxford, 2011.

[52] P. Friedl and D. Gilmour, "Collective cell migration in morphogenesis, regeneration and cancer," *Nat Rev Mol Cell Biol*, vol. 10, no. 7, pp. 445–457, 2009.

[53] D. Thirumalai and R. D. Mountain, "Activated dynamics, loss of ergodicity, and transport in supercooled liquids," *Phys Rev E*, vol. 47, no. 1, p. 479, 1993.

[54] J.-L. Barrat, J.-N. Roux, and J.-P. Hansen, "Diffusion, viscosity and structural slowing down in soft sphere alloys near the kinetic glass transition," *Chem Phys*, vol. 149, no. 1-2, pp. 197–208, 1990.

[55] T. Kirkpatrick and D. Thirumalai, "Colloquium: Random first order transition theory concepts in biology and physics," *Rev Mod Phys*, vol. 87, no. 1, p. 183, 2015.

[56] B. Vorselaars, A. V. Lyulin, K. Karatasos, and M. Michels, "Non-gaussian nature of glassy dynamics by cage to cage motion," *Phys Rev E*, vol. 75, no. 1, p. 011504, 2007.

[57] M. D. Brooks, M. L. Burness, and M. S. Wicha, "Therapeutic implications of cellular heterogeneity and plasticity in breast cancer," *Cell stem cell*, vol. 17, no. 3, pp. 260–271, 2015.

[58] A. Marusyk, V. Almendro, and K. Polyak, "Intra-tumour heterogeneity: a looking glass for cancer?," *Nat Rev Cancer*, vol. 12, no. 5, pp. 323–334, 2012.

[59] J. Toner, "Birth, death, and flight: A theory of malthusian flocks," *Phys Rev Lett*, vol. 108, no. 8, p. 088102, 2012.

[60] V. Almendro, A. Marusyk, and K. Polyak, "Cellular heterogeneity and molecular evolution in cancer," *Annu Rev Pathol*, vol. 8, pp. 277–302, 2013.

[61] R. Hoefflin, B. Lahrmann, G. Warsow, D. Hübschmann, C. Spath, B. Walter, X. Chen, L. Hofer, S. Macher-Goeppinger, Y. Tolstov, *et al.*, "Spatial niche formation but not malignant progression is a driving force for intratumoural heterogeneity," *Nat Comm*, vol. 7, 2016.

[62] D. S. Dean, "Langevin equation for the density of a system of interacting langevin processes," *Journal of Physics A: Mathematical and General*, vol. 29, no. 24, p. L613, 1996.

[63] M. Doi, "Second quantization representation for classical many-particle system," *Journal of Physics A: Mathematical and General*, vol. 9, no. 9, p. 1465, 1976.

[64] L. Peliti, "Path integral approach to birth-death processes on a lattice," *Journal de Physique*, vol. 46, no. 9, pp. 1469–1483, 1985.

[65] A. Gelimson and R. Golestanian, "Collective dynamics of dividing chemotactic cells," *Physical review letters*, vol. 114, no. 2, p. 028101, 2015.

[66] H. S. Samanta and J. Bhattacharjee, "Nonequilibrium statistical physics with fictitious time," *Physical Review E*, vol. 73, no. 4, p. 046125, 2006.

[67] H. S. Samanta, J. Bhattacharjee, and D. Gangopadhyay, "Growth models and models of turbulence: A stochastic quantization perspective," *Physics Letters A*, vol. 353, no. 2, pp. 113–115, 2006.

[68] P. Pathmanathan, J. Cooper, A. Fletcher, G. Mirams, P. Murray, J. Osborne, J. Pitt-Francis, A. Walter, and S. Chapman, "A computational study of discrete mechanical tissue models," *Physical biology*, vol. 6, no. 3, p. 036001, 2009.

[69] E. Palsson and H. G. Othmer, "A model for individual and collective cell movement in dictyostelium discoideum," *Proceedings of the National Academy of Sciences*, vol. 97, no. 19, pp. 10448–10453, 2000.

[70] J. C. Dallon and H. G. Othmer, "How cellular movement determines the collective force generated by the dictyostelium discoideum slug," *Journal of theoretical biology*, vol. 231, no. 2, pp. 203–222, 2004.

[71] E. Palsson, "A three-dimensional model of cell movement in multicellular systems," *Future Generation Computer Systems*, vol. 17, no. 7, pp. 835–852, 2001.

[72] D. Drasdo and S. Höhme, "Individual-based approaches to birth and death in avascular tumors," *Mathematical and Computer Modelling*, vol. 37, no. 11, pp. 1163–1175, 2003.

[73] G. Helmlinger, P. A. Netti, H. C. Lichtenbeld, R. J. Melder, and R. K. Jain, "Solid stress inhibits the growth of multicellular tumor spheroids," *Nature biotechnology*, vol. 15, no. 8, pp. 778–783, 1997.

[74] K. Polyak and R. A. Weinberg, "Transitions between epithelial and mesenchymal states: acquisition of malignant and stem cell traits," *Nature reviews. Cancer*, vol. 9, no. 4, p. 265, 2009.

[75] J. Galle, M. Loeffler, and D. Drasdo, "Modeling the effect of deregulated proliferation and apoptosis on the growth dynamics of epithelial cell populations in vitro," *Biophysical journal*, vol. 88, no. 1, pp. 62–75, 2005.

[76] J. P. Freyer and R. M. Sutherland, "Regulation of growth saturation and development of necrosis in emt6/ro multicellular spheroids by the glucose and oxygen supply," *Cancer research*, vol. 46, no. 7, pp. 3504–3512, 1986.

[77] J. J. Casciari, S. V. Sotirchos, and R. M. Sutherland, "Variations in tumor cell growth rates and metabolism with oxygen concentration, glucose concentration, and extracellular ph," *Journal of cellular physiology*, vol. 151, no. 2, pp. 386–394, 1992.

[78] J. Landry, J. P. Freyer, and R. M. Sutherland, "Shedding of mitotic cells from the surface of multicell spheroids during growth," *Journal of cellular physiology*, vol. 106, no. 1, pp. 23–32, 1981.